Acta Materialia 175 (2019) 250–261

Contents lists available at ScienceDirect

Acta Materialia

journal homepage: www.elsevier.com/locate/actamat

Full length article

Atomistic phase field chemomechanical modeling of dislocation-solute-precipitate interaction in Ni–Al–Co

Jaber Rezaei Mianroodi [a, b, *], Pratheek Shanthraj [a, c], Paraskevas Kontis [a],
Jonathan Cormier [d], Baptiste Gault [a, e], Bob Svendsen [a, b], Dierk Raabe [a]

[a] Microstructure Physics and Alloy Design, Max-Planck-Institut für Eisenforschung, Düsseldorf, Germany
[b] Material Mechanics, RWTH Aachen University, Aachen, Germany
[c] The School of Materials, The University of Manchester, Manchester, UK
[d] Institut Pprime, Physics and Mechanics of Materials Department, UPR CNRS 3346, ISAE-ENSMA, 1 avenue Clément Ader, BP 40109, 86961 Futuroscope-, Chasseneuil, France
[e] Department of Materials, Imperial College, South Kensington, London SW7 2AZ, UK

ARTICLE INFO

Article history:
Received 18 February 2019
Received in revised form
21 May 2019
Accepted 5 June 2019
Available online 13 June 2019

Keywords:
Atomistic phase field chemomechanics
Dislocation glide
Solute segregation
Dislocation-solute interaction
Ni-based superalloys

ABSTRACT

Dislocation-precipitate interaction and solute segregation play important roles in controlling the mechanical behavior of Ni-based superalloys at high temperature. In particular, the increased mobility of solutes at high temperature leads to increased dislocation-solute interaction. For example, atom probe tomography (APT) results [1] for single crystal MC2 superalloy indicate significant segregation of solute elements such as Co and Cr to dislocations and stacking faults in γ' precipitates. To gain further insight into solute segregation, dislocation-solute interaction, and its effect on the mechanical behavior in such Ni-superalloys, finite-deformation phase field chemomechanics [2] is applied in this work to develop a model for dislocation-solute-precipitate interaction in the two-phase γ-γ' Ni-based superalloy model system Ni–Al–Co. Identification and quantification of this model is based in particular on the corresponding Ni–Al–Co embedded atom method (EAM) potential [3]. Simulation results imply both Cottrell- and Suzuki-type segregation of Co in γ and γ'. Significant segregation of Co to dislocation cores and faults in γ' is also predicted, in agreement with APT results. Predicted as well is the drag of Co by γ dislocations entering and shearing γ'. Since solute elements such as Co generally prefer the γ phase, Co depletion in γ' could be reversed by such dislocation drag. The resulting change in precipitate chemistry may in turn affect its stability and play a role in precipitate coarsening and rafting.

1. Introduction

The mechanical behavior of multiphase metallic alloys is strongly influenced by dislocations and their interaction with solutes and other defects. These include point defects (such as vacancies), line defects (other dislocations), surface defects (grain and phase boundaries), and volumetric defects (e.g. precipitates). The details of dislocation interaction with each of these and their effect on dislocation motion depend decisively on factors such as (variations in) temperature, stress, and chemical composition. In the latter case, for example, solute segregation to dislocation cores, i.e., regions of significant lattice distortion and high stress, can result in significant local chemical heterogeneity and spatially varying material properties, affecting dislocation and mechanical behavior [e.g., 4].

An example of materials in which dislocation-solute and dislocation-defect interaction play a significant role is Ni-based superalloys. Given their superior high-temperature creep and fatigue behavior [5–7], Ni-based superalloys are a natural choice for many applications such as turbine blades in jet engines and in land-based power generation gas turbines [5,8]. This is due in large part to their microstructure, consisting in the single crystal case of a face-centered cubic (fcc) γ matrix phase and an $L1_2$ γ' precipitate phase. In particular, the latter are responsible for the significant strength increase of such alloys. The matrix phase is a Ni-based solid solution of elements (e.g., W, Re, Co, Cr) added for further strengthening as well as to adjust misfit and phase equilibrium. The

---

* Corresponding author Material Mechanics, RWTH Aachen University, Aachen, Germany.
E-mail address: j.mianroodi@mpie.de (J.R. Mianroodi).

https://doi.org/10.1016/j.actamat.2019.06.008
1359-6454/

precipitate is mostly Ni_3Al with elements such as Ti and Ta partitioning to it. Significant variation in composition is also observed due to segregation of solutes to dislocation cores and stacking faults [9–11]. For example, Co and Cr are observed to segregate to superlattice intrinsic stacking faults (SISF) inside γ' [10]. The resulting spatial variation in composition can have a strong influence on a number of properties such as elastic stiffness, stacking fault energy, interface energy, or dislocation mobility.

When it comes to dislocation modeling, many approaches ranging from atomistic/quantum level up to mean-field density models have been developed [12–15]. For example, Rodney and Martin [16] studied dislocation interaction with interstitial loops in Ni using molecular dynamics (MD) based on an embedded atom potential. They observed that interstitial clusters are often dragged by the gliding dislocation. As the cluster is dragged by the dislocation, it moves along the dislocation line and reacts with other clusters. Although fully resolving details of dislocation motion and evolution, MD is limited to atomistic length- and timescales, the latter excluding for example solute diffusion. Recent development of hybrid atomistic modeling, e.g., coupled MD and kinetic Monte Carlo [e.g. 17], or diffusive molecular dynamics (DMD) [e.g. 18–20] can overcome this timescale limitation. Another issue for both atomistic and continuum modeling is the availability of an accurate interatomic potential for multi-component system.

Continuum phase field (PF) modeling of dislocation processes [e.g. 21–26] is applicable at larger lengthscale and on longer (e.g., dislocation mobility) timescales. In addition, atomistic PF methods [such as 26,27] are capable of modeling the disregistry field of the dislocation core with atomic accuracy. In the case of Ni-based superalloys, Vorontsov et al. [28] employed phase field microelasticity [e.g. 21–23] to model dislocation interaction with γ' precipitates. For this purpose, they worked with a Fourier-based representation of the stacking fault energy calibrated for both Ni γ and Ni_3Al γ' at constant chemistry. Using this model, they simulated the glide and evolution of a $\langle 112 \rangle a_0$ dislocation ribbon initially in γ driven by loading toward a γ' precipitate. Single dislocation dissociation and related fault formation inside γ' are captured by their model. In later work, Vorontsov et al. [29] developed an effective stacking fault energy model for multiple dislocations and corresponding faults such as (superlattice) extrinsic stacking faults (S)ESF.

In addition to dislocation modeling, PF models are also widely employed to model microstructure evolution and solute diffusion [30,31]. For example, in the case of Ni-based superalloys, Kundin et al. [32] simulated γ' coarsening with the help of such models. To this end, they accounted for the lattice misfit between γ and γ' as well as the corresponding interface energy. To calibrate their model, they used the Thermo-Calc database for Ni alloys. The energy based formulation of PF provides a straightforward way to couple different types of ordering (e.g., phase, lattice plane stacking, chemical). For example, Zhou et al. [33] modeled dislocation shearing of γ' precipitates by coupling dislocation glide and atomic reordering via a long-range order parameter mediating the formation of a SESF as the dislocation enters the precipitate.

In the current work, finite-deformation phase-field chemomechanics [2] is applied to develop a model for dislocation-solute-precipitate interaction in the two-phase γ-γ' Ni-based superalloy model system Ni–Al–Co. The model formulation is presented in Section 2. Energetic material properties of the model are determined atomistically in Section 3 with the help of the Ni–Al–Co embedded atom method (EAM) potential of Purja Pun et al. [3]. For comparison with simulation results, Section 4 begins with a summary of recent results from atom probe tomography on solute segregation to defects during rafting in the γ' phase of an MC2 alloy. The identified model is then applied to the simulation of Co segregation to dislocation cores and to faults in each phase during dissociation of perfect dislocations. Simulation results for Co segregation profiles are qualitatively compared with corresponding atom probe results in γ'. Lastly, dynamic dislocation-solute-precipitate interaction is also investigated for two different initial dislocation configurations. The work ends with a summary in Section 5.

2. Model

The following represents an application of the finite-deformation- and phase-field-based methodology developed in Ref. [2] for the chemomechanics of multiphase, multicomponent solids, and in particular metallic alloy systems. For the phase-field-based modeling of dislocations, this builds in particular on phase field microelasticity [PFM; e.g. 21,23] and its atomistic extension [APFM; e.g. 26,27]. In the current case, the solid consists of a Ni matrix γ phase and a Ni_3Al precipitate γ' phase, both containing Co. First principle calculations [e.g. 34] of site substitution in Ni_3Al imply that Co may occupy both Ni and Al sites, with a weak preference for the Ni sites. As a first approximation, then, any site fractioning of Co in γ' is neglected, both phases are modeled as fcc, and Co replaces Ni randomly in both phases. In addition, Co is assumed to be the only diffusing component for simplicity. In the case of quasi-static, isothermal (i.e., fixed absolute temperature θ) conditions, then, the chemomechanical balance relations

$$\dot{c}_{\mathrm{Co}} = \operatorname{div} M^{\alpha}_{\mathrm{Co}} \nabla \mu^{\alpha}_{\mathrm{Co}} \, , \quad 0 = \operatorname{div} \boldsymbol{P}_{\alpha} \, , \tag{1}$$

for Co mass and linear momentum, respectively, determine the Co concentration field c_{Co} and the deformation field $\boldsymbol{\chi}$, respectively, in each phase $\alpha = \gamma,\gamma'$. Here, M^{α}_{Co} is the (specific) Co diffusivity (mobility), $\mu^{\alpha}_{\mathrm{Co}}$ its (specific) chemical potential, and $\boldsymbol{P}_{\alpha}$ the first Piola-Kirchhoff (PK) stress tensor.

To focus attention on bulk dislocation-solute and dislocation-precipitate interaction in this work, the γ-γ' microstructure is assumed fixed in a corresponding periodic unit cell. Further, for simplicity, the γ-γ' interface is idealized as sharp interface. In this case, the mixture free energy density is purely bulk. The phase free energy density

$$\begin{aligned} &\psi_{\alpha}(c_{\mathrm{Co}}, \boldsymbol{F}, \boldsymbol{F}_{\mathrm{R}\alpha}, \boldsymbol{\varphi}_{\alpha}, \nabla \boldsymbol{\varphi}_{\alpha}) \\ &= \psi^{\mathrm{ch}}_{\alpha}(c_{\mathrm{Co}}) + \psi^{\mathrm{el}}_{\alpha}(c_{\mathrm{Co}}, \boldsymbol{F}, \boldsymbol{F}_{\mathrm{R}\alpha}) + \psi^{\mathrm{sf}}_{\alpha}(c_{\mathrm{Co}}, \boldsymbol{\varphi}_{\alpha}) + \psi^{\mathrm{co}}_{\alpha}(\nabla \boldsymbol{\varphi}_{\alpha}) \end{aligned} \tag{2}$$

($\alpha = \gamma,\gamma'$) consists of chemical $\psi^{\mathrm{ch}}_{\alpha}$, elastic $\psi^{\mathrm{el}}_{\alpha}$, stacking fault $\psi^{\mathrm{sf}}_{\alpha}$, and dislocation core $\psi^{\mathrm{co}}_{\alpha}$ contributions, respectively, with $\boldsymbol{F} = \nabla \boldsymbol{\chi}$ the deformation gradient. The residual local deformation $\boldsymbol{F}_{\mathrm{R}\alpha}$ is due to mechanical and chemical processes resulting in stress relaxation, and $\boldsymbol{\varphi}_{\alpha} := (\varphi^{\alpha}_{1}, \ldots, \varphi^{\alpha}_{n})$ represents an array of order-parameter fields related to dislocation slip (assuming the same number n of these in each phase). The chemical part $\psi^{\mathrm{ch}}_{\alpha}(c_{\mathrm{Co}})$ of ψ_{α} is determined by regular-solution-based homogeneous

$$\begin{aligned} \psi^{\mathrm{ch}}_{\alpha}(c_{\mathrm{Co}}) &= \varepsilon^{\mathrm{ch}}_{\alpha}(c_{\mathrm{Co}}) - \theta \, \eta^{\mathrm{ch}}_{\alpha}(c_{\mathrm{Co}}) \, , \\ \varepsilon^{\mathrm{ch}}_{\alpha}(c_{\mathrm{Co}}) &= \varepsilon^{\alpha}_{0\,\mathrm{Co}} \, c_{\mathrm{Co}} + \varepsilon^{\alpha}_{0\,\mathrm{CoCo}} \, c^{2}_{\mathrm{Co}} \, , \\ \eta^{\mathrm{ch}}_{\alpha}(c_{\mathrm{Co}}) &= \eta^{\alpha}_{0\mathrm{Co}} \, [c_{\mathrm{Co}} \ln c_{\mathrm{Co}} + (1 - c_{\mathrm{Co}}) \ln(1 - c_{\mathrm{Co}})] \, . \end{aligned} \tag{3}$$

Here, $\varepsilon^{\alpha}_{0\,\mathrm{Co}}$ is the (internal) self-energy density with SI units of $\mathrm{J/m^3}$, $\varepsilon^{\alpha}_{0\,\mathrm{CoCo}}$ the (internal) interaction energy density ($\mathrm{J/m^3}$), and $\eta^{\alpha}_{0\,\mathrm{Co}}$ the mixing entropy density ($\mathrm{J/m^3K}$). The elastic contribution

$$\psi^{\mathrm{el}}_{\alpha}(c_{\mathrm{Co}}, \boldsymbol{F}, \boldsymbol{F}_{\mathrm{R}\alpha}) = \frac{1}{2} \, \boldsymbol{E}_{\mathrm{L}\alpha}(\boldsymbol{F}, \boldsymbol{F}_{\mathrm{R}\alpha}) \cdot \mathsf{C}_{\alpha}(c_{\mathrm{Co}}) \, \boldsymbol{E}_{\mathrm{L}\alpha}(\boldsymbol{F}, \boldsymbol{F}_{\mathrm{R}\alpha}) \tag{4}$$

to ψ_{α} is modeled in harmonic form with respect to the elastic stiffness C_{α} assuming $|\boldsymbol{E}_{\mathrm{L}\alpha}| \ll 1$. Here, $\boldsymbol{E}_{\mathrm{L}\alpha} := \frac{1}{2}(\boldsymbol{C}_{\mathrm{L}\alpha} - \boldsymbol{I})$ is the lattice

Green strain, $\boldsymbol{C}_{\mathrm{L}\alpha} := \boldsymbol{F}_{\mathrm{L}\alpha}^{\mathrm{T}}\boldsymbol{F}_{\mathrm{L}\alpha}$ the right Cauchy-Green deformation, and $\boldsymbol{F}_{\mathrm{L}\alpha} := \boldsymbol{F}\boldsymbol{F}_{\mathrm{R}\alpha}^{-1}$ the lattice local deformation. The evolution of $\boldsymbol{F}_{\mathrm{R}\alpha}$ is assumed to be affected by that of both Co content and dislocation slip, resulting in the current finite-deformation context in flow-rule-like relation

$$\dot{\boldsymbol{F}}_{\mathrm{R}\alpha} = \boldsymbol{L}_{\mathrm{R}\alpha}\left(\dot{c}_{\mathrm{Co}}, \dot{\boldsymbol{\varphi}}_{\alpha}\right)\boldsymbol{F}_{\mathrm{R}\alpha}, \quad \boldsymbol{L}_{\mathrm{R}\alpha} = \dot{c}_{\mathrm{Co}}\boldsymbol{H}_{\mathrm{Co}}^{\alpha} + \sum\nolimits_{a=1}^{n}\dot{\varphi}_{a}^{\alpha}\boldsymbol{H}_{\mathrm{gl}a}^{\alpha}. \tag{5}$$

Here, $\boldsymbol{H}_{\mathrm{gl}\ a}^{\alpha} := \boldsymbol{b}_{a}^{\alpha}\otimes\boldsymbol{n}_{a}^{\alpha}/d_{a}^{\alpha}$ is the residual distortion due to dislocation glide with Burgers vector $\boldsymbol{b}_{a}^{\alpha}$, glide-plane normal $\boldsymbol{n}_{a}^{\alpha}$, and glide-plane spacing d_{a}^{α}. In addition, $\boldsymbol{H}_{\mathrm{Co}}^{\alpha}$ is the residual distortion due to the presence of Co. Lastly, (2) is determined by the stacking fault $\psi_{\alpha}^{\mathrm{sf}}(c_{\mathrm{Co}}, \boldsymbol{\varphi}_{\alpha})$ and dislocation core $\psi_{\alpha}^{\mathrm{co}}(\nabla\boldsymbol{\varphi}_{\alpha})$ energies. The former is discussed in detail in the following sections. For simplicity, the latter is approximated here by the geometric linear form

$$\psi_{\alpha}^{\mathrm{co}}(\nabla\boldsymbol{\varphi}_{\alpha}) = \sum\nolimits_{a=1}^{n}\sum\nolimits_{b=1}^{n}\phi_{0ab}^{\alpha}\nabla\varphi_{a}^{\alpha}\boldsymbol{\cdot}\boldsymbol{N}_{ab}^{\alpha}\nabla\varphi_{b}^{\alpha} \tag{6}$$

with $\boldsymbol{N}_{ab}^{\alpha} = (\boldsymbol{b}_{a}^{\alpha}/d_{a}^{\alpha}\boldsymbol{\cdot}\boldsymbol{b}_{b}^{\alpha}/d_{b}^{\alpha})\,[(\boldsymbol{n}_{a}^{\alpha}\boldsymbol{\cdot}\boldsymbol{n}_{b}^{\alpha})\,\boldsymbol{I} - \boldsymbol{n}_{b}^{\alpha}\otimes\boldsymbol{n}_{a}^{\alpha}]$ for the case of planar dislocation cores [e.g. 26].

As carried out in detail in Ref. [2], additional constitutive relations based in particular on relations such as (2) and (5) are formulated in a thermodynamically consistent fashion with the help of the dissipation principle [e.g. 35]. In this context, one obtains in particular the thermodynamically consistent generalization

$$\varrho_{\alpha}\mu_{\mathrm{Co}}^{\alpha} \quad = \quad \partial_{c_{\mathrm{Co}}}\psi_{\alpha}^{\mathrm{ch}} + \partial_{c_{\mathrm{Co}}}\psi_{\alpha}^{\mathrm{el}} + \partial_{c_{\mathrm{Co}}}\psi_{\alpha}^{\mathrm{sf}} - \boldsymbol{F}_{\mathrm{L}\alpha}\boldsymbol{H}_{\mathrm{Co}}^{\alpha}\boldsymbol{F}_{\mathrm{L}\alpha}^{-1}\boldsymbol{\cdot}\boldsymbol{K}_{\alpha} \tag{7}$$

of the Cahn-Hilliard chemical potential for Co from (2), with ϱ_{α} the mass density. Here,

$$\boldsymbol{K}_{\alpha} = \left(\partial_{\boldsymbol{F}}\psi_{\alpha}^{\mathrm{el}}\right)\boldsymbol{F} = \boldsymbol{F}_{\mathrm{L}\alpha}C_{\alpha}[\boldsymbol{E}_{\mathrm{L}\alpha}]\boldsymbol{F}_{\mathrm{L}\alpha}^{\mathrm{T}} \tag{8}$$

is the Kirchhoff stress via (4). As well, one obtains the thermodynamically consistent generalization

$$\phi^{\cdot}{}_{a}^{\alpha} = -m_{a}^{\alpha}\,\nu_{\alpha}\left(\partial_{\varphi_{a}^{\alpha}}\psi_{\alpha}^{\mathrm{sf}} - \boldsymbol{F}_{\mathrm{L}\alpha}\boldsymbol{H}_{\mathrm{gl}\ a}^{\alpha}\boldsymbol{F}_{\mathrm{L}\alpha}^{-1}\boldsymbol{\cdot}\boldsymbol{K}_{\alpha} - \mathrm{div}\partial_{\nabla\varphi_{a}^{\alpha}}\psi_{\alpha}^{\mathrm{co}}\right) \tag{9}$$

($\alpha = \gamma,\gamma'$) of overdamped relaxational (i.e., Ginzburg-Landau) dynamics for ϕ_{a}^{α}, with m_{a}^{α} the corresponding mobility. Lastly, the hyperelastic form

$$\boldsymbol{P}_{\alpha} = \partial_{\boldsymbol{F}}\psi_{\alpha} = \boldsymbol{K}_{\alpha}\boldsymbol{F}^{-\mathrm{T}}, \tag{10}$$

for the first Piola-Kirchhoff stress $\boldsymbol{P}_{\alpha}$ completes the basic thermodynamically consistent constitutive relations of the current chemomechanical model for Ni–Al–Co. For more details on the current modeling approach and methodology, the interested reader is referred to Svendsen et al. [2].

3. Model identification

For simplicity, the phase mass density ϱ_{α} and molar volume Ω_{α} of $\alpha = \gamma,\gamma'$ are assumed constant in this work. With the lattice constants $a_{0}^{\gamma} = 3.52$ Å for Ni and $a_{0}^{\gamma'} = 3.53$ Å for Ni_3Al, we have for example $\Omega_{\gamma} = 6.564 \times 10^{-6}\ \mathrm{m}^3/\mathrm{mol}$ and $\Omega_{\gamma'} = 6.638 \times 10^{-6}\ \mathrm{m}^3/\mathrm{mol}$. Note as well that $\eta_{0\ \mathrm{Co}}^{\alpha} = R/\Omega_{\alpha}$ in (3). Given a_{0}^{α} and choosing $\boldsymbol{\varphi}_{\alpha} = (\varphi_{1}^{\alpha}, \ldots, \varphi_{n}^{\alpha})$, note that $\boldsymbol{b}_{a}^{\alpha}$, $\boldsymbol{n}_{a}^{\alpha}$, d_{a}^{α}, and so $\boldsymbol{H}_{\mathrm{gl}\ a}^{\alpha} = \boldsymbol{b}_{a}^{\alpha}\otimes\ \boldsymbol{n}_{a}^{\alpha}/\ d_{a}^{\alpha}$, are determined for $a = 1, \ldots, n$ and $\alpha = \gamma,\gamma'$. Restricting attention in this work to glide of planar dislocations (cores) on octahedral $\{111\}$ planes in both (Ni,Co) and $(Ni,Co)_3Al$, we then have $\boldsymbol{n}_{a}^{\alpha} \equiv \{111\}/\sqrt{3}$ and $d_{a}^{\alpha} = a_{0}^{\alpha}/\sqrt{3}$. General slip directions in each $\{111\}$ plane can be parameterized by two phase fields, i.e. one ϕ_{110}^{α} in a $\langle 110\rangle$ direction, and a second ϕ_{112}^{α} in a (perpendicular) $\langle 112\rangle$ direction [e.g., 26, 36]. For example, in the (111) plane, ϕ_{110}^{α} is associated with $[\bar{1}10\rangle$, and ϕ_{112}^{α} with $[\overline{11}2\rangle$. In this case, $\boldsymbol{b}_{110}^{\gamma} \equiv a_{0}^{\gamma}\langle 110\rangle/2$ and $\boldsymbol{b}_{112}^{\gamma} \equiv a_{0}^{\gamma}\langle 112\rangle/6$ for γ, as well as $\boldsymbol{b}_{110}^{\gamma'} \equiv a_{0}^{\gamma'}\langle 110\rangle$ and $\boldsymbol{b}_{112}^{\gamma'} \equiv a_{0}^{\gamma'}\langle 112\rangle$ for γ'. Thus, $\boldsymbol{b}_{110}^{\alpha} \equiv a_{0}^{\alpha}\langle 110\rangle/2$, $\boldsymbol{b}_{112}^{\alpha} \equiv a_{0}^{\alpha}\langle 112\rangle/6$, $n = 8$, and $\boldsymbol{\varphi}_{\alpha} = (\varphi_{1}^{\alpha}, \ldots, \varphi_{8}^{\alpha})$ for both phases. Let $\boldsymbol{\varphi} = (\varphi_{1}, \ldots, \varphi_{8})$ represent either one in what follows.

Energetic properties of $\alpha = \gamma, \gamma'$ containing Co are calculated atomistically at 0 K for $c_{\mathrm{Co}} = 0, 0.01, 0.02, \ldots, 0.2$ using the Ni–Al–Co EAM potential of [3] in LAMMPS [37]. These properties include $\varepsilon_{0\ \mathrm{Co}}^{\alpha}$, $\varepsilon_{0\ \mathrm{CoCo}}^{\alpha}$ and $\eta_{0\ \mathrm{Co}}^{\alpha}$ in (3), C_{α} in (4), $\boldsymbol{H}_{\mathrm{Co}}^{\alpha}$ in (5), $\varphi_{0\ ab}^{\alpha}$ in (6), and the stacking fault energy $\psi_{\alpha}^{\mathrm{sf}}$ in (2). Determination of these, the Co mobility M_{Co}^{α} in (1), and the dislocation mobility m_{a}^{α} in (9), is discussed in what follows. When there is no chance of confusion, we dispense with the subscript “Co” to simplify the notation in what follows.

3.1. Elastic properties

Given the cubic symmetry of both γ and γ', C_{γ} and $C_{\gamma'}$ are determined by the three independent Cartesian tensor components C_{1111}^{α}, C_{1122}^{α}, and C_{1212}^{α}. To determine the concentration dependence of these, Ni atoms are replaced randomly with Co and the resulting elastic properties are calculated via molecular statics. The elastic constants are calculated based on small perturbation of the simulation cell size in different directions and calculating the corresponding change in the (virial) stress state. Results for periodic and cubic simulation cells of side length 3.5, 7.0 and 14.0 nm indicate system size independence for 14.0 nm. A fit of the corresponding discrete atomistic results yields

$$\begin{aligned} C_{1111}^{\gamma}(c) &= 1460.4c^2 - 280.3c + 241.3 \\ C_{1122}^{\gamma}(c) &= 1270.0c^2 - 406.3c + 150.7 \\ C_{1212}^{\gamma}(c) &= 1358.2c^2 - 482.4c + 127.0, \end{aligned} \tag{11}$$

and

$$\begin{aligned} C_{1111}^{\gamma'}(c) &= 1761.1c^2 - 575.4c + 235.3 \\ C_{1122}^{\gamma'}(c) &= 878.5c^2 - 286.1c + 165.3 \\ C_{1212}^{\gamma'}(c) &= 750.6c^2 - 369.5c + 129.4, \end{aligned} \tag{12}$$

(all in GPa). These and the discrete atomistic results are shown in Fig. 1.

Note that adding Co randomly to the system induces internal stresses that needs to be relaxed before elastic stiffness calculation are carried out. This is achieved using an initial damped dynamics minimization followed by conjugate gradient with system relaxation under zero stress in all directions.

3.2. Residual distortion due to Co

To calculate the lattice distortion $\boldsymbol{H}^{\alpha}$ for Co in (5) resulting from replacement of Ni by Co, a periodic simulation cell of initial (subscript “0”) size

$$\left(L_{x}^{0}, L_{y}^{0}, L_{z}^{0}\right) = \left(L_{1}^{0}, L_{2}^{0}, L_{3}^{0}\right) = \left(24\sqrt{2}, 12\sqrt{6}, 24\sqrt{3}\right) a_{0}^{\alpha} \tag{13}$$

is used. Here, $\boldsymbol{i}_{x} = \boldsymbol{i}_{1}$ is parallel to $[\bar{1}10]$, $\boldsymbol{i}_{y} = \boldsymbol{i}_{2}$ to $[\overline{11}2]$, and $\boldsymbol{i}_{z} = \boldsymbol{i}_{3}$ to $[111]$. This is the cell for $c = 0$ and zero distortion. For each value of c, the system energy is minimized via conjugate gradient iteration at zero stress in all directions with cell relaxation using the Parrinello-Rahman method [38,39]. The corresponding results for the

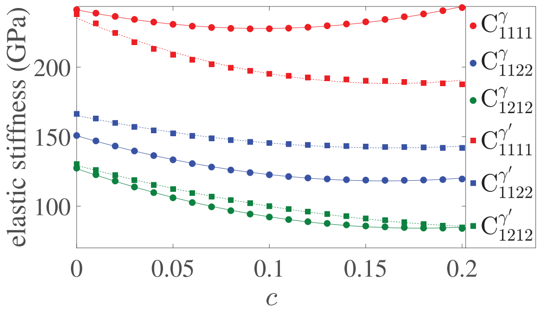

Fig. 1. Atomistic results for C^{α}_{1111} (red), C^{α}_{1122} (blue), and C^{α}_{1212} (green) for $\alpha = \gamma$ (circles) and $\alpha = \gamma'$ (squares) as a function of Co concentration c. The fits in (11) and (12) to these results are shown as same-color curves. (For interpretation of the references to color in this figure legend, the reader is referred to the Web version of this article.)

components of $\boldsymbol{H}^{\alpha}$ for Co are shown in Fig. 2.

Corresponding fits to the atomistic results yield

$$\boldsymbol{H}^{\alpha}(c) = \varepsilon^{\alpha}_{0}\, c\, \boldsymbol{I}\,, \quad \varepsilon^{\gamma}_{0} = 0.0719\,, \quad \varepsilon^{\gamma'}_{0} = 0.0082\,, \tag{14}$$

for Co. The atomistic results shown in Fig. 2 imply that Co does not induce any significant shear distortion in either phase. The three normal distortion components appear to be equal, indicating purely volumetric distortion depending linearly on c. As before, three system sizes are considered to ensure system size independence. Results are shown here for the largest system. Based on these results, residual volumetric distortion due to Co is larger in γ (about 0.014 for $c = 0.2$) compared to γ' (about 0.0016 for $c = 0.2$).

In addition to residual distortion due to the presence of solute such as Co, there is also in general such distortion resulting from lattice misfit between γ and γ'. Since the difference in lattice constants (3.52 Å in γ, 3.53 Å in γ', based on the EAM potential for Ni—Al—Co) is small, and precipitate evolution is not considered in the current work, this misfit contribution to the total residual distortion is neglected here. In addition, in order to focus on particle shearing and solute drag by solute decorated matrix dislocations, we have neglected interface dislocations and changes in precipitate shape in the current work.

3.3. *Fault energies*

Given material symmetry, the fault energies are determined for a single octahedral {111} glide plane in both (Ni,Co) and (Ni,Co)$_3$Al. For this case, the corresponding stacking fault energy density $\psi^{\mathrm{sf}}_{\alpha}$ in (2) takes the form

$$\psi^{\mathrm{sf}}_{\alpha}(c, \phi_{110}, \phi_{112}) = \gamma^{\mathrm{sf}}_{\alpha}(c, \phi_{110}, \phi_{112})/d^{\alpha}_{111}\,. \tag{15}$$

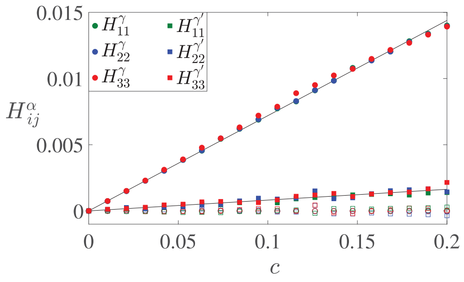

Fig. 2. Atomistic results for the Cartesian components $H^{\alpha}_{ij}(c)$ of $\boldsymbol{H}^{\gamma}(c)$ (circles) and $\boldsymbol{H}^{\gamma'}(c)$ (squares) for Co. In particular, H^{α}_{11} (green fill), H^{α}_{22} (blue fill), H^{α}_{33} (red fill), H^{α}_{12} (green hollow), H^{α}_{13} (blue hollow), H^{α}_{23} (red hollow). The fits in (14) to the normal distortion results are shown (black lines) for comparison. (For interpretation of the references to color in this figure legend, the reader is referred to the Web version of this article.)

In what follows, let $\phi_1 = \phi_{110}$ and $\phi_2 = \phi_{112}$. Fig. 3 displays the fitted $\gamma^{\mathrm{sf}}_{\alpha}(0, \phi_1, \phi_2)$ using the EAM potential of [3] for Ni—Al—Co.

The current model form for $\gamma^{\mathrm{sf}}_{\alpha}(c, \phi_1, \phi_2)$ is based on the generalization (A.1) of the Fourier-series-based representation of [28]. The coefficients $c^{\alpha}_{0}(c), \ldots, c^{\alpha}_{11}(c)$ in (A.1) are determined via least-squares fit to the “data” points calculated from the EAM potential of [3] for Ni—Al—Co. For $c = 0$, these latter points are listed in Tables A.1 and A.2, respectively. The atomistic determination of $\gamma^{\mathrm{sf}}_{\alpha}(c, \phi_1, \phi_2)$ for $c > 0$ is based on periodic simulation cells in which random Ni atoms are replaced by Co up to the desired concentration. The SFE is determined under (cell mean) stress control in the Parrinello-Rahman approach [38]. This is much more robust than free-surface-based relaxation, which results in stress oscillations on the fault plane. As shown in the calculations, the faulted atomic layers at the periodic boundaries have no effect on the results when the system size is large enough. An example of a simulation cell for γ' containing a SISF and Co ($c = 0.19$) is shown in Fig. 4.

To exclude the faulted layer of atoms at the periodic boundary (unknown (red) atoms at the top and bottom of the simulation cell in Fig. 4, top), $\gamma^{\mathrm{sf}}_{\alpha}(c, \phi_1, \phi_2)$ is determined in the dashed region (from $L^{0}_{z}/4$ to $3L^{0}_{z}/4$) in Fig. 4 (top). Different system sizes, as well as ensemble averaging at each c, are employed to ensure independence from system size and Co atom configuration. Using these, $\gamma^{\mathrm{sf}}_{\alpha}(c, \phi_1, \phi_2)$ are determined at fixed ϕ_1,ϕ_2 corresponding to the faults (i.e., ISF, APB, CSF, SISF; see Fig. 3) and shown in Fig. 5.

The fitted results for $\gamma^{\mathrm{sf}}_{\alpha}(c, \phi_1, \phi_2)$ of the chosen faults are given by (in mJ/m^2)

$$\begin{aligned} \gamma^{\mathrm{ISF}}_{\gamma}(c) &= 981.3c^2 + 90.1c + 136.3\,, \\ \gamma^{\mathrm{APB}}_{\gamma'}(c) &= -325.7c^2 - 537.7c + 173.4\,, \\ \gamma^{\mathrm{CSF}}_{\gamma'}(c) &= -166.2c^2 - 231.3c + 229.5\,, \\ \gamma^{\mathrm{SISF}}_{\gamma'}(c) &= -103.8c^2 - 238.2c + 17.8\,. \end{aligned} \tag{16}$$

In turn, these results are employed to determine $c^{\alpha}_{0}(c), \ldots, c^{\alpha}_{11}(c)$ in (A.1) via least-squares fit as summarized in Table A.3. Given this, $\gamma^{\mathrm{sf}}_{\alpha}(c, \phi_1, \phi_2)$ then determines $\psi^{\mathrm{sf}}_{\alpha}(c, \phi_{110}, \phi_{112})$ via (15), and so $\psi^{\mathrm{sf}}_{\alpha}(c, \boldsymbol{\varphi})$ in (2) via material symmetry.

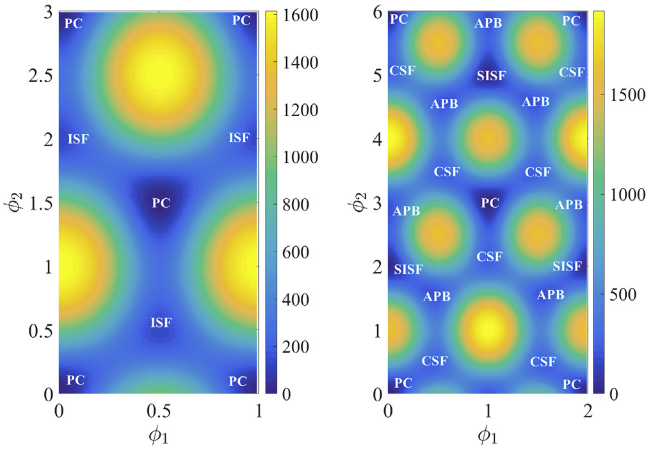

Fig. 3. Fitted $\gamma^{\mathrm{sf}}_{\alpha}(0, \phi_1, \phi_2)$ for Ni ($\alpha = \gamma$; left) and Ni$_3$Al ($\alpha = \gamma'$; right) in units of mJ/m^2. Local minima shown include perfect crystal (PC), intrinsic stacking fault (ISF), complex stacking fault (CSF), anti-phase boundary (APB), and superlattice intrinsic stacking fault (SISF). As done in this figure and in the sequel, the values of ϕ_1 and ϕ_2 are expressed in “units” of $a^{\alpha}_{0}\langle 110\rangle/2$ and $a^{\alpha}_{0}\langle 112\rangle/6$, respectively, in the context of $\gamma^{\mathrm{sf}}_{\alpha}(c, \phi_1, \phi_2)$.

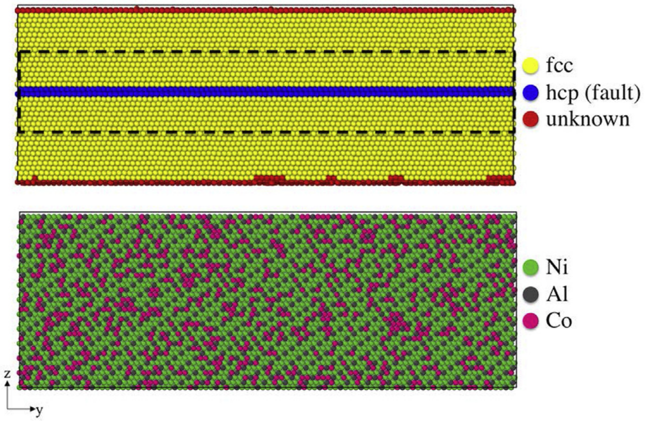

Fig. 4. γ' simulation cell of size $(L_x^0, L_y^0, L_z^0) = (24\sqrt{2}, 24\sqrt{6}, 12\sqrt{3})\, a_0^{\gamma'}$ containing a SISF and Co with $c = 0.19$. Top: common neighbor analysis of lattice structure. Blue (hcp) region represents the SISF. Black dashed region (from $L_z^0/4$ to $3L_z^0/4$) used for energy determination (see text for details). Bottom: atomic distribution. All atomistic results visualized using Ovito [40]. (For interpretation of the references to color in this figure legend, the reader is referred to the Web version of this article.)

3.4. *Chemical energy*

To calculate the internal part $\varepsilon_\alpha^{\text{ch}}(c)$ of $\psi_\alpha^{\text{ch}}(c)$ from (3), Co atoms are again randomly added to the system (without defect) and the corresponding simulation cell is relaxed under zero stress at 0 K. The resulting energy relative to its value at $c = 0$ is shown in Fig. 6. A fit of $\varepsilon_\alpha^{\text{ch}}(c)$ to the atomistic results for Co yields

$$
\begin{array}{rclcrcl}
\Omega_\gamma \varepsilon_{0\ \text{Co}}^{\gamma} & = & -21.45\,, & & \Omega_\gamma \varepsilon_{0\ \text{CoCo}}^{\gamma} & = & -7.7\,, \\
\Omega_{\gamma'} \varepsilon_{0\ \text{Co}}^{\gamma'} & = & -13.66\,, & & \Omega_{\gamma'} \varepsilon_{0\ \text{CoCo}}^{\gamma'} & = & 59.21\,,
\end{array}
\tag{17}
$$

all in kJ/mol. As before, only Co concentrations up to 0.2 is considered here. Bulk phase composition calculation based on CALPHAD and atom probe data on Co concentration in γ and γ' [e.g., 41] imply that Co generally has higher solubility in γ than in γ'. This is captured correctly by the interatomic potential as seen in Fig. 6 with larger energy reduction when Co is dissolved into γ compared to γ' phase.

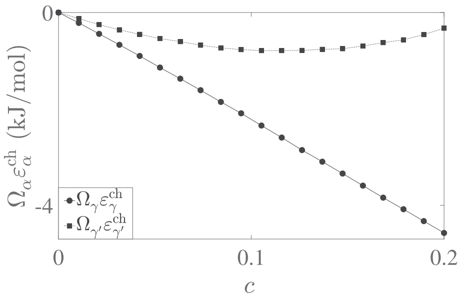

Fig. 6. Atomistic values for the chemical internal energy (per mole) in γ (circles) and γ' (squares). Also shown is the fit (curves) to $\varepsilon_\alpha^{\text{ch}}(c)$ from (3) given in (17).

3.5. *Dislocation core energy*

As discussed at the beginning of Section 3, attention is restricted to planar cores and octahedral slip systems, and these are the same in γ and γ'. Further, slip in each {111} glide plane is parameterized by two phase fields, i.e., ϕ_{110} and ϕ_{112}. Neglecting cross coupling between different {111} planes for simplicity, (6) reduces to a sum of two terms of the form

$$
\begin{array}{rcl}
\psi_{\alpha\,111}^{\text{co}}(\nabla \boldsymbol{\varphi}) & = & \phi_{0\,11}^{\alpha}\, |\boldsymbol{b}_{110}^{\alpha}/d_{111}^{\alpha}|^2\, \nabla\varphi_{110} \cdot (\boldsymbol{I} - \boldsymbol{n}_{111}^{\alpha} \otimes \boldsymbol{n}_{111}^{\alpha}) \nabla\varphi_{110} \\
 & + & \phi_{0\,22}^{\alpha}\, |\boldsymbol{b}_{112}^{\alpha}/d_{111}^{\alpha}|^2\, \nabla\varphi_{112} \cdot (\boldsymbol{I} - \boldsymbol{n}_{111}^{\alpha} \otimes \boldsymbol{n}_{111}^{\alpha}) \nabla\varphi_{112}\,.
\end{array}
\tag{18}
$$

The unknown coefficients $\varphi_{0\ 11}^{\alpha}$ and $\varphi_{0\ 22}^{\alpha}$ are calculated via a fit to disregistry results from molecular statics (MS) for a dissociated edge dislocation, yielding

$$
\begin{array}{rclcrcl}
\varphi_{0\ 11}^{\gamma} \left|\boldsymbol{b}_{110}^{\gamma}/d_{111}^{\gamma}\right|^2 & = & 5.4 \times 10^{11}\,, & & \varphi_{0\ 22}^{\gamma} \left|\boldsymbol{b}_{112}^{\gamma}/d_{111}^{\gamma}\right|^2 & = & 2.1 \times 10^{10}\,, \\
\varphi_{0\ 11}^{\gamma'} \left|\boldsymbol{b}_{110}^{\gamma'}/d_{111}^{\gamma'}\right|^2 & = & 4.8 \times 10^{11}\,, & & \varphi_{0\ 22}^{\gamma'} \left|\boldsymbol{b}_{112}^{\gamma'}/d_{111}^{\gamma'}\right|^2 & = & 1.8 \times 10^{10}\,,
\end{array}
\tag{19}
$$

(all in J/m). With respect to PF-based dislocation modeling, neglect of $\psi_\alpha^{\text{co}}(\nabla\boldsymbol{\varphi})$ corresponds to generalized Peierls-Nabarro [e.g., 42] or phase-field dislocation dynamics [e.g., 24] modeling. For more details in this regard, the interested reader is referred to Ref. [27].

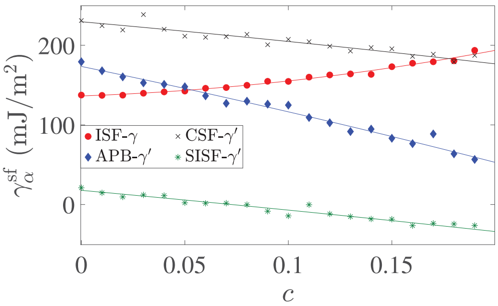

Fig. 5. Atomistically determined stacking fault energy $\gamma_\alpha^{\text{sf}}(c, \phi_1, \phi_2)$ for selected faults in $\alpha = \gamma,\gamma'$. Red circles: ISF in γ. Green asterisks: SISF in γ'. Blue diamonds: APB in γ'. Black crosses: CSF in γ'. Also shown in solid lines are the fitted $\gamma_\alpha^{\text{sf}}(c, \phi_1, \phi_2)$ from (16). (For interpretation of the references to color in this figure legend, the reader is referred to the Web version of this article.)

3.6. *Other model parameters*

The mobility M^γ of Co in $(1)_1$ is modeled here by the transition state relation

$$
M^\gamma(c) = \frac{\Theta}{R\theta}\, e^{\Delta Q^*(c)/R\theta}\,, \quad \Delta Q^* = c\, Q_{\text{Co}} + c_{\text{Ni}}\, Q_{\text{Ni}} + c\, c_{\text{Ni}}\, A_{\text{CoNi}}\,,
\tag{20}
$$

from Ref. [43], with

$$
\begin{aligned}
Q_{\mathrm{Co}} &= -286175 - 76.0\,\theta\,, \\
Q_{\mathrm{Ni}} &= -284169 - 67.6\,\theta\,, \\
A_{\mathrm{CoNi}} &= 10787 - 11.5\,\theta\,,
\end{aligned}
\tag{21}
$$

in units of J/mol as a function of θ [T in 43]. Here, Θ is the product of the squared atomic jump distance and the jump frequency. Campbell et. al. [43] assume $\Theta = 1\ \mathrm{m}^2/\mathrm{s}$. Given for example $\theta = 1323$ K, $c = 0.068$, and $c_{\mathrm{Ni}} = 0.63$ (corresponding to the equilibrium concentration of Co and Ni in γ phase of MC2 alloy), note that $M^{\gamma} = 3.82 \times 10^{-15}\ \mathrm{m}^2\mathrm{mol/Js}$. The diffusion coefficient of Co in γ' at $\theta = 1323$ K is about $\tilde{D}^{\gamma'} = 6.2 \times 10^{-16}\ \mathrm{m}^2/\mathrm{s}$ [44] while $\tilde{D}^{\gamma} = 1.4 \times 10^{-15}\ \mathrm{m}^2/\mathrm{s}$ [45]. Based on these, as an estimate, $M^{\gamma'} = M^{\gamma}\tilde{D}^{\gamma'}/\tilde{D}^{\gamma} = 1.69 \times 10^{-15}\ \mathrm{m}^2\mathrm{mol/Js}$ is used for the Co mobility in γ'. Note that the concentration dependency of mobility is ignored in both phases.

Depending on temperature, stress, microstructure, and other factors, dislocations may be more or less mobile than solutes. In the dislocation-solute interaction simulations to be discussed in the next section, the dislocations are not subject to external loading, and this does not play a role. On the other hand, in the dislocation-solute-precipitate interaction simulations, the dislocations are subject to such loading. In the context of the Co mobility model (20), the “empirical” choice $m_a^{\alpha} = 10^{-9}\ \mathrm{m}^3/\mathrm{Js}$ for the dislocation mobility in (9) enables Co segregation/redistribution (resulting in enrichment, depletion) around such gliding dislocations on the timescale of the simulations. This corresponds to a slow moving dislocation either due to interaction with defects or slow external loading rate. A detailed comparison of the interplay between the two material timescales represented by M^{α} and m_a^{α}, and its effect on dislocation-solute and dislocation-solute-precipitate interaction, represents work in progress.

4. Results and discussion

4.1. Atom probe tomography results for solute segregation to defects in MC2

For the purpose of qualitative comparison with the simulation results to be discussed below, solute segregation to defects under non-isothermal creep conditions was investigated in the single-crystal Ni-based MC2 alloy Ni-9.3Cr-5.1Co-1.3Mo-2.6 W-11.2Al-1.9Ti-2.0Ta (at.%) via atom probe tomography (APT). The creep tests in this study were conducted at constant specimen load of 120 MPa for the following thermal cycle in the rafting regime: 15 min at 1323 K + 1 min at 1378 K + 15 min at 1323 K + 1 min at 1433 K [see 1]. Non-isothermal conditions are relevant to real in-service engine conditions. In addition, isothermal tests are generally insufficient for investigation of the deformation and durability of such superalloys [46,47]. APT specimens were prepared from site-specific lift-outs from rafted γ' precipitates and analyzed with a Cameca LEAP 5000XR instrument. The specimens were analyzed in laser mode at a base temperature of 50 K, laser pulse energy 45 pJ, and repetition rate of 125 kHz. Data reconstruction and processing was performed using Cameca IVAS 3.8.2. Fig. 7 displays a typical APT reconstruction of a rafted γ' precipitate containing the trace of compositional variations related to the presence of structural defects [1,48,49].

As shown in Fig. 7 (bottom left, bottom right), Co and Cr segregate to defects in the rafted γ' precipitate. In particular, in both profiles (indicated by arrows) in Fig. 7 (bottom), up to 10 at.% Co enrichment in the defects is evident. On the basis of APT alone, it is not possible to determine the nature of the defect to which this segregation occurred. This requires correlative transmission electron microscopy (TEM) and APT characterization, which represents work in progress. For the current MC2 alloy, determining the defect type is challenging because dislocations are not straight through the cross section of the specimens, in contrast for example to CoNi-based alloys [e.g., 50–52]. Given no independent (e.g., TEM) information on the nature of the defects, as well as the differences in the alloy's composition, no detailed or quantitative comparison with the simulation results below is possible. The qualitative agreement with the simulation is however readily visible. In addition, as will be discussed in more detail below, in this context, the defect in Fig. 7 (bottom left) is interpreted as a dissociated $\langle 110\rangle$ perfect superdislocation (Fig. 10, left). Likewise, the defect in Fig. 7 (bottom right) is interpreted as a dissociated $\langle 112\rangle$ partial superdislocation (Fig. 10, right).

4.2. Dislocation-solute interaction in γ

As a first application of the current model, consider the simulation of Co segregation to dislocations in γ. For this and the other cases to follow, attention is focused on purely bulk behavior in a periodic unit cell containing dislocations on a single {111} glide plane. Consequently, only two phase fields are active ($n = 2$), and $\boldsymbol{\varphi}$=(ϕ_1,ϕ_2) for both phases. The initial dislocation configuration is a dipole; in γ for example, this consists of two perfect $\frac{1}{2}\langle 110\rangle$ monopoles with ($\phi_1 = 1$,$\phi_2 = 0$) in Fig. 3 (left) for each monopole. The Co concentration is initially homogeneous with $c = 0.068$ (i.e., the equilibrium Co concentration in γ phase of the MC2 alloy above). Relaxation of this initial configuration at $\theta = 1323$ K (i.e., as in the non-isothermal creep tests on MC2 discussed above) and zero deformation is simulated via staggered solution of Co mass balance $(1)_1$, mechanical equilibrium $(1)_2$, and overdamped phase field dynamics (9) as implemented in DAMASK [53]. Since dislocation evolution on one glide plane is investigated here, only two order parameters ϕ_1 and ϕ_2 are required to fully describe the slip configuration. As discussed above, dislocation mobility m_a^{α} is set low enough for Co redistribution to occur during dissociation

$$
\frac{1}{2}\left\langle 110\right\rangle \rightarrow \frac{1}{6}\left\langle 112\right\rangle + \mathrm{ISF} + \frac{1}{6}\left\langle 112\right\rangle \tag{22}
$$

of each perfect monopole into two $\frac{1}{6}\langle 112\rangle$ Shockley partials and an intrinsic stacking fault (ISF), resulting in the spatial redistribution of Co shown in Fig. 8.

In the current model, the driving force for this redistribution (and segregation) is the gradient $\nabla\mu^{\alpha}$ of the Co phase chemical potential

$$
\varrho_{\alpha}\mu^{\alpha} = \partial_c\psi_{\alpha}^{\mathrm{ch}} + \partial_c\psi_{\alpha}^{\mathrm{sf}} + \partial_c\psi_{\alpha}^{\mathrm{el}} - \varepsilon_0^{\alpha}\, c\, \boldsymbol{I}\boldsymbol{\cdot}\boldsymbol{K}_{\alpha} \tag{23}
$$

from (7) and $(14)_1$ driving Co mass flux $-M^{\alpha}\nabla\mu^{\alpha}$ in the Co mass balance relation $(1)_1$. For the current simulation case of a single dislocation ($n = 2$),

$$
\nabla\mu^{\alpha} = (\partial_c\mu^{\alpha})\,\nabla c + (\nabla\boldsymbol{F}_{\mathrm{L}\alpha})^{\mathrm{T}}\partial_{\boldsymbol{F}_{\mathrm{L}\alpha}}\mu^{\alpha} + (\partial_{\phi_1}\mu^{\alpha})\,\nabla\phi_1 + (\partial_{\phi_2}\mu^{\alpha})\,\nabla\phi_2 \tag{24}
$$

is obtained from (23), and

$$
\begin{aligned}
\varrho_{\alpha}\partial_c\mu^{\alpha} &= \partial_c\left(\partial_c\psi_{\alpha}^{\mathrm{ch}} + \partial_c\psi_{\alpha}^{\mathrm{sf}} + \partial_c\psi_{\alpha}^{\mathrm{el}}\right) - \varepsilon_0^{\alpha}\ \boldsymbol{I}\boldsymbol{\cdot}(\boldsymbol{K}_{\alpha} + c\,\partial_c\boldsymbol{K}_{\alpha})\,, \\
\varrho_{\alpha}\partial_{\boldsymbol{F}_{\mathrm{L}\alpha}}\mu^{\alpha} &= \partial_c\boldsymbol{P}_{\mathrm{L}\alpha} - \varepsilon_0^{\alpha}\ c\,\boldsymbol{P}_{\mathrm{L}\alpha} - \varepsilon_0^{\alpha}\ c\,\left(\partial_{\boldsymbol{F}_{\mathrm{L}\alpha}}\boldsymbol{P}_{\mathrm{L}\alpha}\right)[\boldsymbol{F}_{\mathrm{L}\alpha}]\,, \\
\varrho_{\alpha}\partial_{\phi_a}\mu^{\alpha} &= \partial_{\phi_a}\partial_c\psi_{\alpha}^{\mathrm{sf}}\,,
\end{aligned}
\tag{25}
$$

via (2), with $\boldsymbol{P}_{\mathrm{L}\alpha} := \partial_{\boldsymbol{F}_{\mathrm{L}\alpha}}\psi_{\alpha}^{\mathrm{el}} = \boldsymbol{K}_{\alpha}\boldsymbol{F}_{\mathrm{L}\alpha}^{-\mathrm{T}}$ the lattice first Piola-Kirchhoff stress. Given (24) for $\nabla\mu^{\alpha}$, we conclude that, in general, spatial variations in c, $\boldsymbol{F}_{\mathrm{L}\alpha}$, ϕ_1 and ϕ_2 will drive Co redistribution and in

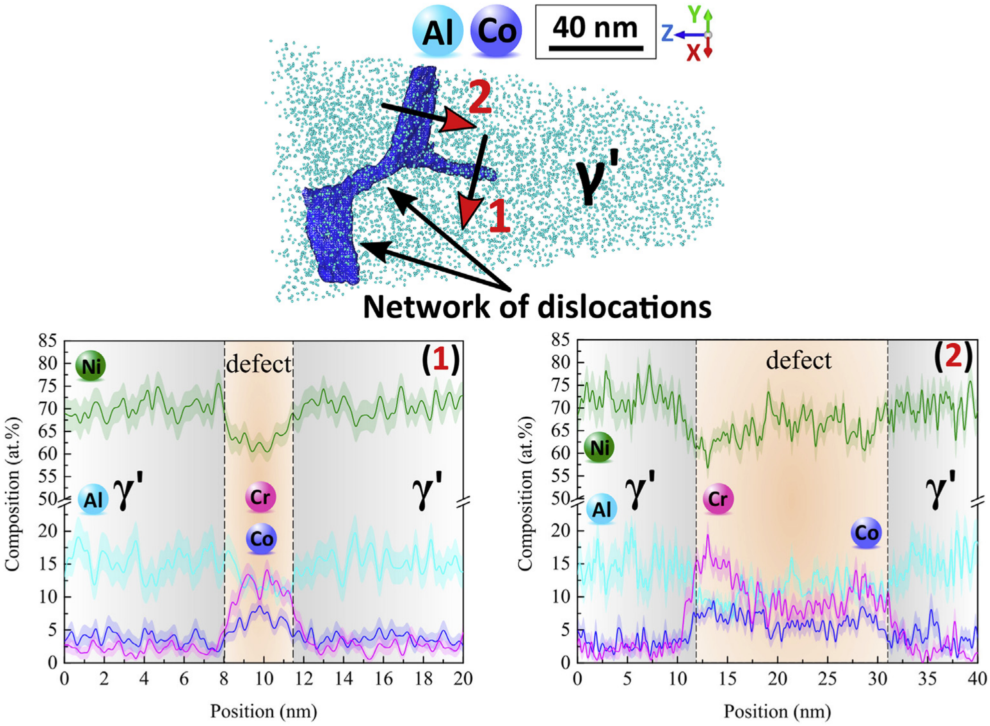

Fig. 7. APT reconstruction of a rafted γ' precipitate with defects. Top: part of a dislocation network (violet) visualized via the 5.0 at.% Co isocomposition surface. Defects are shown as a network of tubular features with local enrichment in Co of up to about 10 at.%. Bottom: concentration profiles along arrow 1 (left) and arrow 2 (right). Error bands around each concentration profile correspond to the 2σ atom probe counting error. (For interpretation of the references to color in this figure legend, the reader is referred to the Web version of this article.)

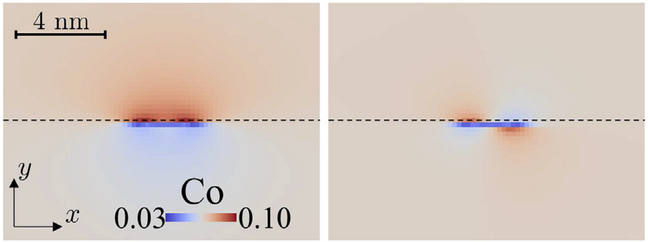

Fig. 8. Co concentration field around a dissociated edge (left) and screw (right) dislocation monopole in γ. Shown is a cross section in the (x,y) plane with y normal to the glide plane. The dislocation line lies along z. The dashed lines represent the $\langle 111\rangle$ plane adjacent to glide plane. In the edge case (left), this is the plane of maximum Co concentration (red). Maximum Co concentration for edge and screw dislocations is 0.096 and 0.087, respectively. Minimum Co concentration for edge and screw dislocations is 0.037 and 0.038, respectively. (For interpretation of the references to color in this figure legend, the reader is referred to the Web version of this article.)

particular segregation.

Note the dependence of μ^α and $\partial_c\mu^\alpha$ on the “hydrostatic” part $\boldsymbol{I}\cdot\boldsymbol{K}_\alpha$ (i.e., trace) of $\boldsymbol{K}_\alpha$. As is well-known, even when the core and non-linearity are neglected [e.g., in the Volterra case: 54,36], edge and screw dislocations have quite different hydrostatic stress fields. This difference is certainly one reason for the different resulting Co distributions in the dissociated edge (left) and screw (right) cases in Fig. 8. More generally, in the current non-linear model accounting for the core, both the hydrostatic and deviatoric parts of $\boldsymbol{K}_\alpha$ contribute in general to Co segregation, for example through the dependence of $\partial_{\boldsymbol{F}_{\mathrm{L}\alpha}}\mu^\alpha$ in $(25)_2$ on $\boldsymbol{P}_{\mathrm{L}\alpha}$.

The results in Fig. 8 are based in particular on the assumption that $\nabla c = 0$ initially. On the other hand, $\nabla\boldsymbol{F}_{\mathrm{L}\alpha}$ and $\nabla\phi_a$ are non-zero in the (initial and dissociated) dislocation core regions in Fig. 8. Consequently, these gradients drive initial Co redistribution. The corresponding coefficients $\partial_{\boldsymbol{F}_{\mathrm{L}\alpha}}\mu^\alpha$ and $\partial_{\phi_a}\mu^\alpha$ in (24) for $\nabla\mu^\alpha$ are determined by the stress $\boldsymbol{P}_{\mathrm{L}\alpha}$ and material properties $\partial_c\boldsymbol{P}_{\mathrm{L}\alpha}$, $\partial_{\boldsymbol{F}_{\mathrm{L}\alpha}}\boldsymbol{P}_{\mathrm{L}\alpha}$, and $\partial_{\phi_a}\partial_c\psi_\alpha^{\mathrm{sf}}$. Even if we had neglected the c dependence of ψ entirely, note that $\partial_{\boldsymbol{F}_{\mathrm{L}\alpha}}\mu^\alpha$ would still be non-zero because lattice distortion due to Co contributes to $\boldsymbol{L}_{\mathrm{R}\alpha}$ from (5). As shown in Fig. 8, the resulting Co redistribution, i.e., depletion (negative segregation) or enrichment (positive segregation) in relation to the surrounding lattice, is more pronounced in the dissociated edge case (left). In addition, in the dissociated screw case (right), note that the opposite edge components of the partials result in Co enrichment above and below the glide plane. On the other hand, in the edge case (left), we have Co depletion on and below the glide plane, and enrichment above.

Fig. 9 shows the dislocation core structure (black solid lines) and Co concentration profile (red lines) for the dissociated edge (left) and screw (right) dislocations from Fig. 8.

Relative to its initial value of 6.8 at.%, in the edge case (left), Co enriches to about 9.6 at.% just above the (planar) cores, and to about 8.6 at.% just above the ISF, on the $\langle 111\rangle$ plane adjacent to glide plane (dashed line in Fig. 8, left). In contrast, on the glide plane itself (just below the dashed curve in Fig. 8, left), Co depletes in the cores and in the ISF. In particular the latter is expected from the fact that $\gamma_\gamma^{\mathrm{ISF}}(c)$ increases with c (Fig. 5, red circles). From (24) and (25), $\partial_c\partial_c\psi_\alpha^{\mathrm{sf}}$ in $\varrho_\alpha\partial_c\mu^\alpha$, and $\partial_{\phi_a}\partial_c\psi_\alpha^{\mathrm{sf}}$ in $\varrho_\alpha\partial_{\phi_a}\mu^\alpha$, are the contributions of $\psi_\alpha^{\mathrm{sf}}$ to the driving force for Co segregation. As shown by the results in Fig. 5, the driving force for Co segregation to the ISF in γ is of negative Suzuki type [55]. On the other hand, Co segregation to the faults in γ' generally results in energy reduction and so a positive Suzuki effect. As well, the increase of $\gamma_\gamma^{\mathrm{ISF}}(c)$ with c results in a change of Shockley partial separation. Indeed, partial separation in the edge case decreases from 18.8 to 17.7 Å during Co segregation. This is also true for the screw case, in which the partial separation

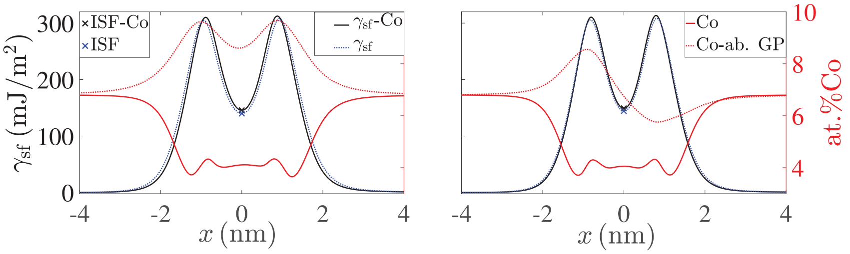

Fig. 9. Fault energy and Co concentration profiles for dissociated edge (left) and screw (right) monopoles. Solid black curve: fault energy with Co. Dashed blue curve: fault energy without Co. Crosses: ISF. Red-dashed curve: Co concentration profile along the dashed line (above glide plane) in Fig. 8. Red curve: Co concentration profile along the glide plane. (For interpretation of the references to color in this figure legend, the reader is referred to the Web version of this article.)

decreases from 16.3 to 15.9 Å, less pronounced than in the edge case because of the lower Co at.%.

4.3. Dislocation-solute interaction in γ'

As implied by a comparison of the γ and γ' fault energy landscapes in Fig. 3, additional dissociation paths are available in γ'. Here, dissociation of $\langle 110\rangle$ perfect, and $\langle 112\rangle$ partial, superdislocations are considered. For example,

$$[110] \rightarrow \frac{1}{6}[211] + \mathrm{CSF} + \frac{1}{6}[12\bar{1}] + \mathrm{APB} + \frac{1}{6}[211] + \mathrm{CSF} + \frac{1}{6}[12\bar{1}] \tag{26}$$

(along ϕ_1 axis in Fig. 3, right) in the former case, and

$$\begin{aligned}[1\bar{1}2] \quad \rightarrow \quad & \frac{1}{6}[211] + \mathrm{CSF} + \frac{1}{6}[1\bar{1}2] + \mathrm{APB} + \frac{1}{6}[\overline{121}] \\ + \quad & \mathrm{SISF} + \frac{1}{6}[1\bar{1}2] + \mathrm{APB} + \frac{1}{6}[211] + \mathrm{CSF} \\ + \quad & \frac{1}{6}[1\bar{1}2] + \mathrm{APB} + \frac{1}{6}[\overline{121}] + \mathrm{CSF} + \frac{1}{6}[1\bar{1}2]\end{aligned} \tag{27}$$

(along ϕ_2 axis in Fig. 3, right) in the latter. Both are scaled by $a_0^{\gamma'}$. Again referring to Fig. 3 (right), the former corresponds to the initial conditions ($\phi_1 = 2, \phi_2 = 0$), and the latter to those ($\phi_1 = 0, \phi_2 = 6$). The temperature is set to $\theta = 1323$ K and the system is relaxed under zero load as before. The dislocation line in both cases is along $[1\bar{1}2]$. Initial uniform Co concentration is set to 3.16 at.% corresponding to the equilibrium Co concentration in γ' phase of MC2 alloy. The resulting fault energy and Co profiles along the glide plane are displayed in Fig. 10 (left) for (26) and in Fig. 10 (right) for (27).

From the atomistic results for $\boldsymbol{H}^{\alpha}(c)$ in (14), lattice distortion due to Co in γ' is almost an order of magnitude smaller than in γ. Consequently, stress-field driven ("Cottrell") segregation is much less pronounced in γ'. As shown in Fig. 10 (left), Co segregation of up to 9.1 at.% to faults (and in particular to the APB) takes place upon dissociation (26) of a $\langle 110\rangle$ superdislocation for an initially uniform Co distribution of 3.16 at.%. Co segregation to the faults results in Co depletion to 3.14 at.% in the γ' matrix surrounding the dissociated dislocation. Since the simulation cell (ca. 65 nm in length) is larger than the region shown in Fig. 10, segregation to the dislocation has relatively little effect on Co concentration. As expected from Fig. 5, as well as from $\gamma_{\gamma'}^{\rm CSF}(c)$ and $\gamma_{\gamma'}^{\rm APB}(c)$ in (16), Co segregation to the CSFs and in particular to the APB results in a significant fault energy reduction. In addition, comparing the fault energy curves with Co (solid black) and without Co (dashed blue), one sees that reduction in APB energy due to Co segregation allows the partials to move further apart. In particular, separation between the two partials bounding the APB region increases from 24.9 to 25.9 Å in this case. Likewise, separation between the first and last partials increases from 54.7 to 55.4 Å during segregation.

Qualitatively similar trends are evident in Fig. 10 (right) for the dissociation (27) of a $\langle 112\rangle$ partial superdislocation. For this case, Co is generally more enriched in the faults than in the dislocation cores, and maximal in the APB (up to 9.2 at.%), corresponding to the largest reduction in fault energy. Fault energy levels are also influenced by the fact that they interact with their bounding partials and adjacent faults. Since these differ in (27), the resulting energy levels for a given fault type can differ as well. This interaction also plays a role in determining fault width and bounding partial separation. For example, consider the two partials bounding the SISF (hollow circle) in Fig. 10 (right). Although Co segregation to the SISF results in energy reduction, the separation of the bounding partials, and so the SISF width, actually decreases from 28.7 to 27.0 Å. This somewhat surprising behavior is due to the interaction with the two bounding APBs. Indeed, this SISF width reduction is accompanied by an increase in APB width from 17.4 to 17.5 and 19.2 to 20.0 Å. As indicated by the results in Fig. 5 as well as by $\gamma_{\gamma'}^{\rm SISF}(c)$ and $\gamma_{\gamma'}^{\rm APB}(c)$ from (16), the decrease in APB energy due to Co is

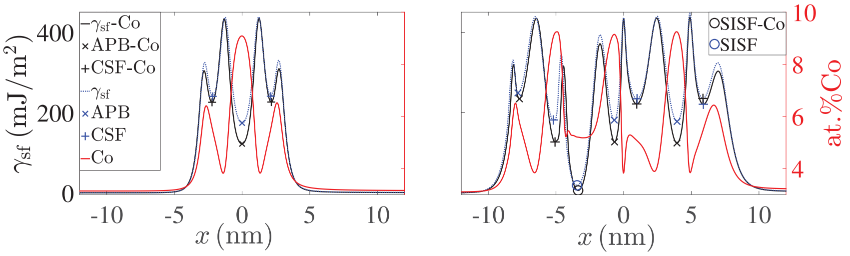

Fig. 10. Fault energy and segregated Co profiles for (26) (left) and (27) (right) along the glide plane. Solid black curve: fault energy with Co. Dashed blue curve: fault energy without Co. Pluses: CSF. Crosses: APB. Circle: SISF. See Fig. 3 (right). Red curve: segregated Co concentration profile. See text for details. (For interpretation of the references to color in this figure legend, the reader is referred to the Web version of this article.)

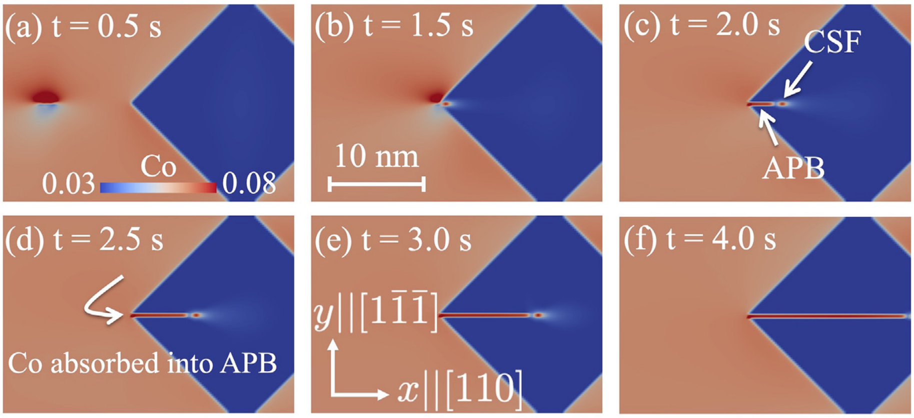

Fig. 11. Snapshots of an $a_0^\gamma\langle 110\rangle/2$ edge dislocation interacting with a precipitate and the related Co concentration. The dislocation line and glide plane normal are along the z and y axes, respectively. Dislocation motion is deformation controlled up to a shear deformation of $F_{xy} = 0.07$. To better highlight details, Co concentration contours are limited to concentrations between 0.03 and 0.08. See text for details.

stronger than that of the SISF energy. Consequently, APB expansion results in a larger energy reduction than SISF expansion.

Despite the overall reduction in fault energy when Co is added, the overall length of the superdislocation is almost unchanged at 151.2 Å. This could be related to reduced elastic interaction between partials due to Co (relaxing the dislocation stress field) as well as to the decrease in elastic stiffness (Fig. 1) with increasing Co content.

As discussed above in the context of the APT results, the defect in Fig. 7 (bottom left) is interpreted as a dissociated ⟨110⟩ superdislocation (Fig. 10, left). Likewise, the defect in Fig. 7 (bottom right) is interpreted as a dissociated ⟨112⟩ superdislocation (Fig. 10, right). In both cases, the levels of Co enrichment in the defects (of order 10 at.%) due to segregation is similar. The distance between the first and last concentration peaks in Fig. 10 (left and right) is 55.4 and 151.2 Å respectively. This qualitatively agrees with the widths (35 and 200 Å) of Co enriched regions in the APT results in Fig. 7 (left and right), respectively. Such agreement is perhaps surprising given the differences between the experimental and characterization conditions on the one hand, and the assumptions underlying identified model on the other (e.g., temperature). A more quantitative comparison, contingent for example on additional TEM-based investigation of defects types, as well as on an extension of the current model to include Cr, represents work in progress.

4.4. Dislocation-solute-precipitate interaction

Lastly, we consider the interaction of dislocations with Co which glide from the γ matrix into a γ' precipitate. To this end, a straight edge dislocation of type $a^\gamma\langle 110\rangle/2$ is placed in γ phase. The system also has a square shaped γ' precipitate of size 16 nm with its center located about 24 nm away from the initial dislocation position. Characterization results in Ref. [47] show that the precipitates are cuboidal (before rafting sets in). Other than intersecting the precipitate, the choice of dislocation glide plane is physically arbitrary. Given the symmetry of the simulation cell, the glide plane intersecting the precipitate corner was chosen.

As above, the initial Co concentration is at 6.8 and 3.16 at.% in γ and γ' phases, respectively, and the temperature uniform at $\theta = 1323$ K. The system is then "loaded" under deformation control up to $F_{xy} = 0.07$ (simple shear), driving the dislocation toward the precipitate. Since deformation is controlled, the stress state fluctuates around a shear stress driving the dislocation glide of about 1.7 GPa. This load level is chosen here to drive precipitate shearing. Note that the microscopic load level is often higher that the macroscopic load due to local fluctuations and stress concentration. As discussed above, the dislocation mobility is chosen to be sufficiently small to facilitate Co redistribution. Snapshots of this during dislocation motion and interaction with the precipitate are shown in Fig. 11.

As seen in Fig. 11 (a), and expected from the solubility results above, Co depletes in the precipitate and enriches in the matrix. The equilibrium Co concentration inside the precipitate is about 0.03. The stacking fault width in the dissociated dislocation is small, and the stress field of the dissociated dislocation is close to that of a perfect edge, with positive and negative hydrostatic stress above and below the dislocation, respectively. Since the residual strain due to Co in γ is positive, an increase in Co is seen in regions of positive hydrostatic stress, resulting in a Cottrell atmosphere around the dislocation in Fig. 11 (a).

As the dislocation reaches the precipitate in Fig. 11 (b), note that part of the segregated Co is dragged into the precipitate, and the rest remains at the interface. Since $a_0^\gamma\langle 110\rangle/2$ is not a superdislocation in γ', further glide of the dislocation leaves behind an extended APB (Fig. 11(c–f)) bounded by the interface. This APB can absorb Co from the γ phase. The excess Co at the interface in (b) is transferred into the precipitate and the APB grows in (f). Since the residual strain due to Co in γ' is relatively small, there is no visible Cottrell atmosphere around the dislocation core in γ'. Instead, most of the dragged Co segregates to the APB and narrower CSF.

Lastly, consider the results for precipitate shear by two $a_0^\gamma\langle 110\rangle/2$ matrix dislocations in Fig. 12.

As expected, this combination results in a superdislocation in γ'; consequently, the APB is closed when the second dislocation enters the precipitate (Fig. 12 (d)). Similar to the previous case, Co segregates to the positive hydrostatic regions around the matrix dislocations (Fig. 12 (a)). The two edge dislocations have the same sign and repel each other, but under external loading, both glide toward the precipitate. The first dislocation enters the precipitate (Fig. 12 (b)), depositing Co at the interface, which is absorbed by the APB (Fig. 12 (c)). Termination of the APB by the second dislocation results in deposition of Co from the second dislocation at the interface (Fig. 12 (d)). This deposited Co eventually diffuses back into the matrix as the superdislocation glides away from the interface into the precipitate (Fig. 12 (e) and (f)).

5. Summary

In this work, finite-deformation phase-field (PF) chemomechanics [2] is applied to develop a model for dislocation-solute-precipitate interaction in the two-phase Ni-based superalloy model

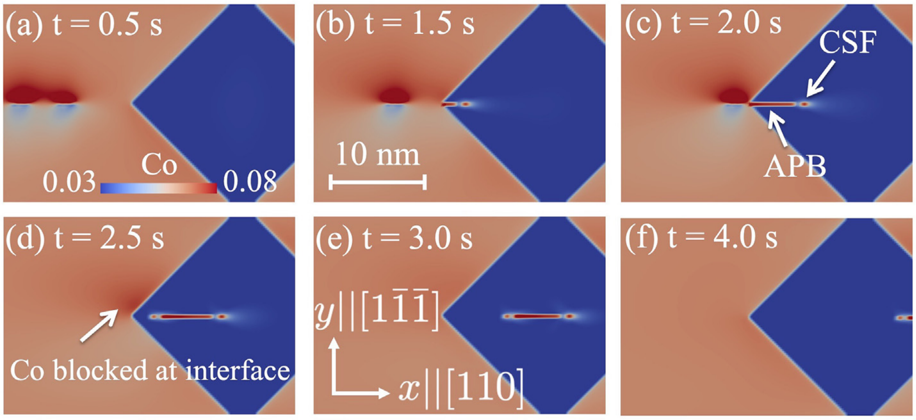

Fig. 12. Snapshots of two $a^{\gamma}\langle 110\rangle/2$ edge dislocations interacting with a precipitate. Simulation and visualization details are the same as described in the caption of Fig. 11.

system Ni–Al–Co. To this end, the model is determined atomistically using the EAM potential for Ni–Al–Co of [3]. In particular, this facilitates quantitative determination of energetic material properties such as elastic stiffness, solute residual distortion, stacking fault energy, and solubility, as well as their dependence on Co content. This dependence results in a strong coupling of dislocation (core) evolution and solute segregation.

As shown by the example simulations, the current model is able to predict coupled dislocation (core) evolution and solute segregation in qualitative agreement with observations on solute segregation from atom probe tomography. The same approach can be applied to more complicated alloys with additional chemical degrees of freedom with parameters fitted to density functional theory results and/or CALPHAD data. As shown for the current Ni–Al–Co model system, the interplay between chemistry and dislocation configuration can explain experimentally observed phenomena such as segregation to dislocations and faults in γ and γ'. These result in compositional changes which may destabilize for example the latter and result in precipitate coarsening.

Acknowledgements

Financial support of the modeling and simulation work reported on here in Subproject M5 of the Priority Program 1713 “Chemomechanics” of the Deutsche Forschungsgemeinschaft (DFG) is gratefully acknowledged. We thank SAFRAN Helicopter Engines, France, for providing MC2 alloy. P.K., B.G. and D.R. are grateful to the MPG for the funding of the Laplace project. P.S. thanks the EPSRC for financial support through the associated programme grant LightFORM (EP/R001715/1) and the Airbus -University of Manchester Centre for Metallurgical Excellence for supporting aspects of this research. Uwe Tezins and Andreas Sturm are also acknowledged for their support on APT experiments.

A. Concentration-dependent fault energy

The details of the generalized stacking fault energy surface is presented in this appendix. The surface energy is parameterized based on Fourier representation as employed by Ref. [28]. However, the coefficients are assumed to be concentration dependent.

$$
\begin{aligned}
&\gamma_{\alpha}^{\mathrm{sf}}(c,\phi_1,\phi_2)\\
&= c_0^{\alpha}(c)+c_1^{\alpha}(c)[\cos(p\phi_2)+\cos(0.5p\phi_2+0.5q\phi_1)+\cos(0.5p\phi_2-0.5q\phi_1)]\\
&+c_2^{\alpha}(c)[\cos(q\phi_1)+\cos(1.5p\phi_2+0.5q\phi_1)+\cos(1.5p\phi_2-0.5q\phi_1)]\\
&+c_3^{\alpha}(c)[\cos(2p\phi_2)+\cos(p\phi_2+q\phi_1)+\cos(p\phi_2-q\phi_1)]\\
&+c_4^{\alpha}(c)[\cos(2.5p\phi_2+0.5q\phi_1)+\cos(2p\phi_2+q\phi_1)+\cos(0.5p\phi_2+1.5q\phi_1)]\\
&+c_4^{\alpha}(c)[\cos(0.5p\phi_2-1.5q\phi_1)+\cos(2p\phi_2-q\phi_1)+\cos(2.5p\phi_2-0.5q\phi_1)]\\
&+ c_5^{\alpha}(c)[\cos(3p\phi_2)+\cos(1.5p\phi_2+1.5q\phi_1)+\cos(1.5p\phi_2-1.5q\phi_1)\}\\
&+c_6^{\alpha}(c)[\cos(4p\phi_2)+\cos(2p\phi_2+2q\phi_1)+\cos(2p\phi_2-2q\phi_1)]\\
&+c_7^{\alpha}(c)[\sin(p\phi_2)-\sin(0.5p\phi_2+0.5q\phi_1)-\sin(0.5p\phi_2-0.5q\phi_1)]\\
&+c_8^{\alpha}(c)[\sin(2p\phi_2)-\sin(p\phi_2+q\phi_1)-\sin(p\phi_2-q\phi_1)]\\
&+c_9^{\alpha}(c)[\sin(2.5p\phi_2+0.5q\phi_1)-\sin(2p\phi_2+q\phi_1)-\sin(0.5p\phi_2+1.5q\phi_1)]\\
&-c_9^{\alpha}(c)[\sin(0.5p\phi_2-1.5q\phi_1)+\sin(2p\phi_2-q\phi_1)+\sin(2.5p\phi_2-0.5q\phi_1)]\\
&+c_{10}^{\alpha}(c)[\sin(3p\phi_2)-\sin(1.5p\phi_2+1.5q\phi_1)-\sin(1.5p\phi_2-1.5q\phi_1)]\\
&+c_{11}^{\alpha}(c)[\sin(4p\phi_2)-\sin(2p\phi_2+2q\phi_1)-\sin(2p\phi_2-2q\phi_1)],
\end{aligned}
\tag{A.1}
$$

Table A.1
Points on the SFE surface of Ni (γ) calculated from the EAM potential of [3] for Ni–Al–Co used to determine $c_0^{\gamma}(0),\ldots,c_{11}^{\gamma}(0)$ in (A.1) via least-squares fit. All energy values are in mJ/m^2. In particular, these values include the intrinsic stacking fault (ISF) energy (*).

ϕ_1	0	0.5	0	0	0	0
ϕ_2	0	0.5	0.25	0.5	0.75	1
$\gamma_{\gamma}^{\mathrm{sf}}$	0	136.2*	262.1	949.6	1485.6	1614.9
ϕ_1	0.125	0.25	0.375	0.375	0.25	0.125
ϕ_2	0.125	0.25	0.375	0.625	0.75	0.875
$\gamma_{\gamma}^{\mathrm{sf}}$	136.9	292.5	243.5	367.7	974.2	1491.5

Table A.2

: Points on the SFE surface of Ni_3Al (γ') calculated from the EAM potential of [3] for Ni–Al–Co used to determine $c_0^{\gamma'}(0), \ldots, c_{11}^{\gamma'}(0)$ in (A.1) via least-squares fit. All energy values are in mJ/m^2. In particular, these values represent (i) the superlattice intrinsic stacking fault (SISF) energy (*), (ii) the anti-phase boundary (APB) energy (), and (iii) the complex stacking fault (CSF) energy (+).

ϕ_1	0	0	0	0	0	0	0.45	0.45
ϕ_2	0	1	2	2.9	4	5.1	0.45	1.55
$\gamma_{\gamma'}^{sf}$	0	1634.8	17.7^*	177.5	1918.0	229.1^+	229.1^+	177.5
ϕ_1	0.5	0.55	0.55	0.5	1	1	1	1
ϕ_2	2.5	3.45	4.55	5.5	1	2.1	3	4
$\gamma_{\gamma'}^{sf}$	1634.8	229.1^+	177.5	1634.7	1918.0	229.1^+	0	1634.8
ϕ_1	1	1	1.55	1.55	1.5	1.45	1.45	1.5
ϕ_2	5	5.9	0.45	1.55	2.5	3.45	4.55	5.5
$\gamma_{\gamma'}^{sf}$	17.7^*	177.5	229.1^+	177.5	1634.7	229.1^+	177.5	1634.7

Table A.3

: Atomistically determined Co concentration dependence of $c_0^{\alpha}(c), \ldots, c_{11}^{\alpha}(c)$ in (A.1). All values are in mJ/m^2.

	$\alpha = \gamma$	$\alpha = \gamma'$
$c_0^{\alpha}(c)$	$899.5c^2 + 82.6c + 701.3$	$-119.8c^2 - 190.7c + 687.2$
$c_1^{\alpha}(c)$	-211.0	$-18.6c^2 - 24.5c - 104.9$
$c_2^{\alpha}(c)$	-37.9	$4.9c^2 + 3.7c + 26.8$
$c_3^{\alpha}(c)$	$-81.8c^2 - 7.5c + 11.4$	$-29.6c^2 - 48.1c - 164.7$
$c_4^{\alpha}(c)$	$-81.8c^2 - 7.5c + 3.3$	$35.2c^2 + 58.4c + 33.5$
$c_5^{\alpha}(c)$	$-81.8c^2 - 7.5c - 1.3$	$23.5c^2 + 33.4c - 40.7$
$c_6^{\alpha}(c)$	$27.3c^2 + 2.5c - 1.6$	$-10.7c^2 - 17.7c - 12.4$
$c_7^{\alpha}(c)$	-310.5	$-2.9c^2 + 10.4c + 75.9$
$c_8^{\alpha}(c)$	-23.8	$-21.4c^2 - 32.3c - 271.1$
$c_9^{\alpha}(c)$	1.5	0.0
$c_{10}^{\alpha}(c)$	-0.8	$14.6c^2 + 28.7c + 33.6$
$c_{11}^{\alpha}(c)$	0.1	$1.5c^2 + 3.1c + 18.7$

References

[1] P. Kontis, Z. Li, D.M. Collins, J. Cormier, D. Raabe, B. Gault, The effect of chromium and cobalt segregation at dislocations on nickel-based superalloys, Scripta Mater. 145 (2018) 76–80.

[2] B. Svendsen, P. Shanthraj, D. Raabe, Finite-deformation phase-field chemomechanics for multiphase, multicomponent solids, J. Mech. Phys. Solids 112 (2018) 619–636.

[3] G.P. Purja Pun, V. Yamakov, Y. Mishin, Interatomic potential for the ternary Ni-Al-Co system and application to atomistic modeling of the B2-L10 martensitic transformation, Model. Simul. Mater. Sci. Eng. 23 (6) (2015) 65006.

[4] A.H. Cottrell, B.A. Bilby, Dislocation theory of yielding and strain ageing of iron, Proc. Phys. Soc. 62 (1) (1949) 49.

[5] R.C. Reed, The Superalloys: Fundamentals and Applications, Cambridge University Press, 2006.

[6] C. Meid, M. Eggeler, P. Watermeyer, A. Kostka, T. Hammerschmidt, R. Drautz, G. Eggeler, M. Bartsch, Stress-induced formation of TCP phases during high temperature low cycle fatigue loading of the single-crystal Ni-base superalloy ERBO/1, Acta Mater. 168 (2019) 343–352.

[7] X. Wu, S.K. Makineni, P. Kontis, G. Dehm, D. Raabe, B. Gault, G. Eggeler, On the segregation of Re at dislocations in the γ' phase of Ni-based single crystal superalloys, Materialia 4 (2018) 109–114.

[8] F. Nabarro, F. de Villiers, Physics of Creep and Creep-Resistant Alloys, Taylor & Francis, 1995.

[9] Y. Koizumi, T. Nukaya, S. Suzuki, S. Kurosu, Y. Li, H. Matsumoto, K. Sato, Y. Tanaka, A. Chiba, Suzuki segregation in Co-Ni-based superalloy at 973 K: an experimental and computational study by phase-field simulation, Acta Mater. 60 (6–7) (2012) 2901–2915.

[10] G.B. Viswanathan, R. Shi, A. Genc, V.A. Vorontsov, L. Kovarik, C.M.F. Rae, M.J. Mills, Segregation at stacking faults within the γ' phase of two Ni-base superalloys following intermediate temperature creep, Scripta Mater. 94 (2015) 5–8.

[11] Y. Rao, T.M. Smith, M.J. Mills, M. Ghazisaeidi, Segregation of alloying elements to planar faults in γ'-Ni3Al, Acta Mater. 148 (2018) 173–184.

[12] M. Ghazisaeidi, D. Trinkle, Core structure of a screw dislocation in Ti from density functional theory and classical potentials, Acta Mater. 60 (3) (2012) 1287–1292.

[13] M.C. Fivel, Discrete dislocation dynamics: an important recent break-through in the modelling of dislocation collective behaviour, Compt. Rendus Phys. 9 (3–4) (2008) 427–436.

[14] J.R. Mianroodi, R. Peerlings, B. Svendsen, Strongly non-local modelling of dislocation transport and pile-up, Phil. Mag. 96 (12) (2016) 1171–1187.

[15] T. Hochrainer, S. Sandfeld, M. Zaiser, P. Gumbsch, Continuum dislocation dynamics: towards a physical theory of crystal plasticity, J. Mech. Phys. Solids 63 (2014) 167–178.

[16] D. Rodney, G. Martin, Dislocation pinning by glissile interstitial loops in a nickel crystal: a molecular-dynamics study, Phys. Rev. B Condens. Matter 61 (13) (2000) 8714–8725.

[17] V. Turlo, T.J. Rupert, Dislocation-assisted linear complexion formation driven by segregation, Scripta Mater. 154 (2018) 25–29.

[18] J. Li, S. Sarkar, W. Cox, T. Lenosky, E. Bitzek, Y. Wang, Diffusive molecular dynamics and its application to nanoindentation and sintering, Phys. Rev. B 84 (5) (2011) 1–8.

[19] J.P. Mendez, M. Ponga, M. Ortiz, Diffusive molecular dynamics simulations of lithiation of silicon nanopillars, J. Mech. Phys. Solids 115 (2018) 123–141.

[20] M. Ponga, D. Sun, A unified framework for heat and mass transport at the atomic scale, Model. Simul. Mater. Sci. Eng. 26 (3) (2018), 035014.

[21] Y.U. Wang, Y.M. Jin, A.M. Cutiño, A.G. Khachaturyan, Nanoscale phase field microelasticity theory of dislocations: model and 3d simulations, Acta Mater. 49 (2001) 1847–1857.

[22] C. Shen, Y. Wang, Incorporation of gamma-surface to phase field model of dislocations: simulation dislocation dissociation in fcc crystals, Acta Mater. 52 (2004) 683–691.

[23] Y. Wang, J. Li, Phase field modeling of defects and deformation, Acta Mater. 58 (2010) 1212–1235.

[24] A. Hunter, I.J. Beyerlein, T.C. Germann, M. Koslowski, Influence of the stacking fault energy surface on partial dislocations in fcc metals with a three dimensional phase field dynamics model, Phys. Rev. B 84 (2011) 144108.

[25] A. Hunter, R.F. Zhang, I.J. Beyerlein, T.C. Germann, M. Koslowski, Dependence of equilibrium stacking fault width in fcc metals on the γ-surface, Model. Simul. Mater. Sci. Eng. 21 (2013) 25015.

[26] J.R. Mianroodi, B. Svendsen, Atomistically determined phase-field modeling of dislocation dissociation, stacking fault formation, dislocation slip, and reactions in fcc systems, J. Mech. Phys. Solids 77 (2015) 109–122.

[27] J.R. Mianroodi, A. Hunter, I.J. Beyerlein, B. Svendsen, Theoretical and computational comparison of models for dislocation dissociation and stacking fault/core formation in fcc crystals, J. Mech. Phys. Solids 95 (2016) 719–741.

[28] V. Vorontsov, C. Shen, Y. Wang, D. Dye, C. Rae, Shearing of γ' precipitates by a <112> dislocation ribbons in Ni-base superalloys: a phase field approach, Acta Mater. 58 (12) (2010) 4110–4119.

[29] V.A. Vorontsov, R.E. Voskoboinikov, C.M. Rae, Shearing of γ' precipitates in Ni-base superalloys: a phase field study incorporating the effective γ-surface, Phil. Mag. 92 (5) (2012) 608–634.

[30] C. Schwarze, A. Gupta, T. Hickel, R. Darvishi Kamachali, Phase-field study of ripening and rearrangement of precipitates under chemomechanical coupling, Phys. Rev. B 95 (17) (2017) 1–14.

[31] R. Darvishi Kamachali, C. Schwarze, Inverse ripening and rearrangement of precipitates under chemomechanical coupling, Comput. Mater. Sci. 130 (2017) 292–296.

[32] J. Kundin, L. Mushongera, T. Goehler, H. Emmerich, Phase-field modeling of the γ'-coarsening behavior in Ni-based superalloys, Acta Mater. 60 (9) (2012) 3758–3772.

[33] N. Zhou, C. Shen, M.J. Mills, J. Li, Y. Wang, Modeling displacive-diffusional coupled dislocation shearing of γ' precipitates in Ni-base superalloys, Acta Mater. 59 (9) (2011) 3484–3497.

[34] A.V. Ruban, H.L. Skriver, Calculated site substitution in γ'-Ni3Al, Solid State Commun. 99 (11) (1996) 813–817.

[35] M. Šilhavý, The Mechanics and Thermodynamics of Continuous Media, Springer, Berlin, 1997.

[36] V. Bulatov, W. Cai, Computer Simulations of Dislocations, Oxford University Press, 2006.

[37] S. Plimpton, Fast parallel algorithms for short-range molecular dynamics, J. Comput. Phys. 117 (1) (1995) 1–19.

[38] M. Parrinello, A. Rahman, Polymorphic transitions in single crystals: a new molecular dynamics method, J. Appl. Phys. 52 (12) (1981) 7182.

[39] W. Shinoda, M. Shiga, M. Mikami, Rapid estimation of elastic constants by molecular dynamics simulation under constant stress, Phys. Rev. B 69 (13) (2004) 134103.

[40] A. Stukowski, Visualization and analysis of atomistic simulation data with OVITO–the Open Visualization Tool, Model. Simul. Mater. Sci. Eng. 18 (1) (2010), 015012.

[41] S.C. Llewelyn, K.A. Christofidou, V.J. Araullo-Peters, N.G. Jones, M.C. Hardy, E.A. Marquis, H.J. Stone, The effect of Ni:Co ratio on the elemental phase partitioning in γ-γ' Ni-Co-Al-Ti-Cr alloys, Acta Mater. 131 (2017) 296–304.

[42] Y. Xiang, H. Wei, P. Ming, W. E, A generalized Peierls-Nabarro model for curved dislocations and core structures of dislocation loops in Al and Cu, Acta Mater. 56 (2008) 1447–1460.

[43] C. Campbell, W. Boettinger, U. Kattner, Development of a diffusion mobility database for Ni-base superalloys, Acta Mater. 50 (4) (2002) 775–792.

[44] Y. Minamino, S.B. Jung, T. Yamane, K. Hirao, Diffusion of cobalt, chromium, and titanium in Ni3Al, Metallurgical Transactions A 23 (10) (1992) 2783–2790.

[45] S.B. Jung, T. Yamane, Y. Minamino, K. Hirao, H. Araki, S. Saji, Interdiffusion and its size effect in nickel solid solutions of Ni-Co, Ni-Cr and Ni-Ti systems, J. Mater. Sci. Lett. 11 (20) (1992) 1333–1337.

[46] J. Cormier, M. Jouiad, F. Hamon, P. Villechaise, X. Milhet, Very high temperature creep behavior of a single crystal Ni-based superalloy under complex thermal cycling conditions, Phil. Mag. Lett. 90 (8) (2010) 611–620.

[47] J. Cormier, X. Milhet, J. Mendez, Non-isothermal creep at very high temperature of the nickel-based single crystal superalloy MC2, Acta Mater. 55 (18) (2007) 6250–6259.

[48] M. Kuzmina, M. Herbig, D. Ponge, S. Sandlöbes, D. Raabe, Linear complexions: confined chemical and structural states at dislocations, Science 349 (6252) (2015) 1080–1083.

[49] S. Hamadi, F. Hamon, J. Delautre, J. Cormier, P. Villechaise, S. Utada, P. Kontis, N. Bozzolo, Consequences of a room-temperature plastic deformation during processing on creep durability of a Ni-based SX superalloy, Metall. Mater. Trans. A: Physical Metallurgy and Materials Science 49 (9) (2018) 4246–4261.

[50] S.K. Makineni, M. Lenz, P. Kontis, Z. Li, A. Kumar, P.J. Felfer, S. Neumeier, M. Herbig, E. Spiecker, D. Raabe, B. Gault, Correlative microscopy—novel methods and their applications to explore 3D chemistry and structure of nanoscale lattice defects: a case study in superalloys, JOM 70 (9) (2018) 1736–1743.

[51] S.K. Makineni, A. Kumar, M. Lenz, P. Kontis, T. Meiners, C. Zenk, S. Zaefferer, G. Eggeler, S. Neumeier, E. Spiecker, D. Raabe, B. Gault, On the diffusive phase transformation mechanism assisted by extended dislocations during creep of a single crystal CoNi-based superalloy, Acta Mater. 155 (2018) 362–371.

[52] S.K. Makineni, M. Lenz, S. Neumeier, E. Spiecker, D. Raabe, B. Gault, Elemental segregation to antiphase boundaries in a crept CoNi-based single crystal superalloy, Scripta Mater. 157 (2018) 62–66.

[53] F. Roters, M. Diehl, P. Shanthraj, P. Eisenlohr, C. Reuber, S.L. Wong, T. Maiti, A. Ebrahimi, T. Hochrainer, H.-O. Fabritius, S. Nikolov, M. Friák, N. Fujita, N. Grilli, K.G.F. Janssens, N. Jia, P.J.J. Kok, D. Ma, F. Meier, E. Werner, M. Stricker, D. Weygand, D. Raabe, DAMASK–The Düsseldorf Advanced Material Simulation Kit for modeling multi-physics crystal plasticity, thermal, and damage phenomena from the single crystal up to the component scale, Comput. Mater. Sci. 158 (2019) 420–478.

[54] J.P. Hirth, J. Lothe, Theory of Dislocations, second ed., Wiley, New York, 1982.

[55] H. Suzuki, Chemical Interaction of Solute Atoms with Dislocations, Science Reports of the Research Institutes, vol. 4, Tohoku University, 1952, pp. 455–463. Ser. A, Physics, chemistry and metallurgy.